ORIGINAL PAPER

Study of deformation and shape recovery of NiTi nanowires under torsion

Cheng-Da Wu · Po-Hsien Sung · Te-Hua Fang

Abstract The nanomechanical properties, deformation, and shape recovery mechanism of NiTi nanowires (NWs) under torsion are studied using molecular dynamics simulations. The effects of loading rate, aspect ratio of NWs, and NW shape are evaluated in terms of atomic trajectories, potential energy, torque required for deformation, stress, shear modulus, centro-symmetry parameter, and radial distribution function. Simulation results show that dislocation nucleation starts from the surface and then extends to the interior along the {110} close-packed plane. For a high loading rate, the occurrence of torsional buckling of a NW is faster, and the buckling gradually develops near the location of the applied external loading. The critical torsional angle and critical buckling angle increase with aspect ratio of the NWs. Square NWs have better mechanical strength than that of circular NWs due to the effect of shape. Shape recovery naturally occurs before buckling.

Keywords Buckling · Deformation · Molecular dynamics · Nanomechanical properties · NiTi nanowires · Shape recovery

Introduction

NiTi alloy, also called nitinol (for nickel, titanium, and NOL) [1], is a typical shape memory alloy (SMA). SMAs are novel materials which have the ability to return to their predetermined shape when heated to above the transition temperature via a mechanism called the shape memory

C.-D. Wu · P.-H. Sung · T.-H. Fang (✉)
Department of Mechanical Engineering, National Kaohsiung University of Applied Sciences, Kaohsiung 807, Taiwan
e-mail: fang.tehua@msa.hinet.net

effect (SME). Another unique property of SMAs is their superelasticity (SE) (up to a recoverable strain of 15 %). NiTi alloy is widely used in aeronautical [2], biomedical engineering [3, 4], and seismological applications due to its great biocompatibility, mechanical and chemical properties, and near-room-temperature transition. These applications range from the prosaic, for use in mobile phone antennae and eyeglass frames, to cutting-edge roles in biomedical implants [5], actuation [6], and noise control. The SME and the transition temperature depend on the stoichiometry between Ni and Ti atoms. For example, the transition temperature often decreases with increasing Ni content. At the atomic level, the shape memory behavior is related to the phase transformation between austenite (a stable body-centered cubic (bcc) structure at high temperature; B2 cubic structure) and martensite (consisting of randomly oriented variants; B19 structure) via the three-dimensional cooperative movement of atoms (diffusionless). The phase transformation occurs after heating and cooling processes, in which the direction of all variants is reset, recovering the original shape.

Although many experimental studies have been conducted on NiTi alloy [7–9], theoretical studies on the mechanical properties, deformation, and shape recovery mechanism are very limited. Molecular dynamics (MD) simulation is a powerful tool for studying material behavior. It provides detailed deformation information at the atomic level. Atomic simulation avoids experimental noise and turbulence problems and can be used to analyze atomic trajectories and thermodynamic properties. Many nanosystems have been analyzed using MD, such as nanoimprinting [10], nanomultilayers [11] and carbon nanotubes [12] under bending, and dip-pen nanolithography [13, 14]. Zeng et al. [15] studied the relationship between melting temperature and pressure of NiTi alloy. They found that the melting temperature

is about 1575 K under a pressure of 100 kPa, and the melting temperature increases with pressure. Sato et al. [16] studied the microscopic mechanism of the phase transformation of NiTi alloy and found that the changes in stress and martensite ratio during tensile loading are independent of the strain rate. Liang et al. [17] found both the SME and SE in single-crystal face-centered cubic Cu, Ni, and Au nanowires (NWs). These wires can undergo recoverable elongations of up to 50 % under tensile loading and unloading.

We hope the study can contribute to understanding the nanomechanical properties, deformation, and shape recovery mechanism of NiTi NWs under torsion for applications of micro- and nano-systems. The effects of loading rate, aspect ratio of NWs, and NW shape are studied using MD simulations. The results are discussed in terms of atomic trajectories, potential energy, torque required for the deformation, stress, shear modulus, centro-symmetry parameter (CSP), and radial distribution function ($g(r)$).

Methodology

Figure 1 shows the developed three-dimensional MD physical model of a NiTi NW. NWs with a constant diameter (D) of 5 nm and lengths (L) of 10–75 nm are considered. The crystal unit of NiTi NWs in the austenite phase is a bcc structure (B2 structure) with the X-, Y-, and Z- axes in the [100], [010], and [001] directions, respectively. The NW consists of two kinds of
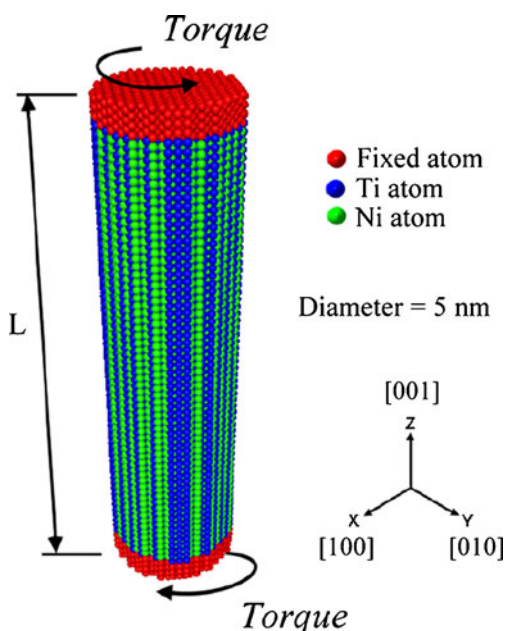

Fig. 1 Schematic MD model of a NiTi NW. The NW is deformed by torsional loading applied to its two ends along the z-direction

atom, namely thermostat atoms and boundary atoms (rigid atoms) at the two ends. The boundary atoms are used to apply external loadings and can support the whole NW. A pair of torsional loads is continuously applied to the two ends of the NW in opposite directions to deform it. The thermostat atoms obey Newton's second law and their velocities are adjusted to maintain the atoms in an isothermal state of 300 K. A Cartesian coordinate system is used in the proposed system without any periodic boundary conditions. The origin is at the center of the lowermost-left atom of the NW. During the torsional test, a total torsional angle (θ) of 360° is used (i.e., a rotation cycle at each end of the NW).

The second-moment approximation of the many-body tight-binding (TB) potential [18] is adopted to describe Ni/Ni and Ti/Ti interactions, and the mixed rule is used for Ni/Ti interaction. The prediction of some properties by the TB method has been proven to be more accurate than that obtained with the embedded atom method (EAM) [19]. Moreover, the computation algorithm associated with the TB method is simpler than that used for the EAM.

The TB potential is expressed as:

$$ES = \sum_i \left(E_R^i + E_B^i \right), \tag{1}$$

where E_B^i and E_R^i denote the bond-structure energy and repulsive energy of atom i, respectively; they are respectively expressed as:

$$E_B^i = -\left\{ \sum_{j \neq i} \xi^2 \cdot \exp\left(-2q\left(\frac{r_{ij}}{r_0} - 1 \right) \right) \right\}^{\frac{1}{2}} \tag{2}$$

$$E_R^i = \sum_j A \cdot \exp\left(-p\left(\frac{r_{ij}}{r_0} - 1 \right) \right), \tag{3}$$

where r_{ij} is the distance between atoms i and j, r_0 is the first-neighbor distance, and A, ξ, p, and q are adjustable parameters governing the interaction between the atoms. The related parameters are listed in Table 1 [18]. The radical distribution function ($g(r)$) [20] describes how the atomic

Table 1 Tight-binding potential parameters used in the simulation [18]

Parameter	A (eV)	ξ(eV)	p	q	r_0(nm)
Ni-Ni	0.104	1.591	11.198	2. 413	0.249
Ti-Ti	0.153	1.879	9.253	2.513	0.295
Ni-Ti	0.300	2.480	7.900	3.002	0.261

density varies as a function of the distance away from one particular atom, which can often be used to identify the crystal order. The $g(r)$ function is defined as

$$g(r) = \frac{N(r, \Delta r)}{\frac{1}{2} N \rho V(r, \Delta r)}, \qquad (4)$$

where N is the total number of atoms, V is the system volume, ρ is the number density ($\rho = N/V$), $N(r, \Delta r)$ is the number of atoms found in a spherical shell of radius r and thickness Δr, with the shell centered on another atom, and $V(r, \Delta r)$ is the volume of the spherical shell.

The time integration of motion is performed using Gear's fifth-order predictor-corrector method with a time step of 1 fs. To increase calculation efficiency, the Verlet neighbor-list method is used. The lists of neighbor atoms are calculated every 10 time steps with a cut-off radius of 0.65 nm.

Results and discussion

Torsional deformation mechanism

For a NW under torsion, planar networks of screw dislocations perpendicular [21, 22] or parallel [23] to the applied torque form to relieve the applied torque. Figure 2 (a) and (b) show the variation of the average potential energy per atom with the θ value and snapshots of the deformation process of the NW under torsion, respectively. The NW has a length of 20 nm. A constant loading rate of 1° ps^{-1} is applied on each of its ends to deform it. The color of the atoms in Fig. 2 (a) and (b) represents the magnitude of their potential energy and CSP [24], respectively. The CSP can be used to readily distinguish whether an atom is near a defect. In Fig. 2 (a), the potential energy (E_p) initially significantly increases with the θ value to an angle of 37° (which is the critical torsional angle (θ_{cr})). The growth of the energy curve follows the following parabolic form: $E_p \propto \theta^2$. The increase of potential energy indicates that the torque required for the deformation increases. The NW within this period undergoes a linear-elastic deformation, which means that the deformation will recover if the loading is removed from the NW [25, 26]. A θ_{cr} value of about 37° has been found for perfect Cu and Al NWs [26, 27] under a similar loading rate. The energy required to deform NiTi NWs is much larger than that required for Cu [26] and Al [27] NWs due to the stronger bonding energy in NiTi NWs. When the θ value exceeds θ_{cr}, the energy curve abruptly drops, which indicates that the NW releases
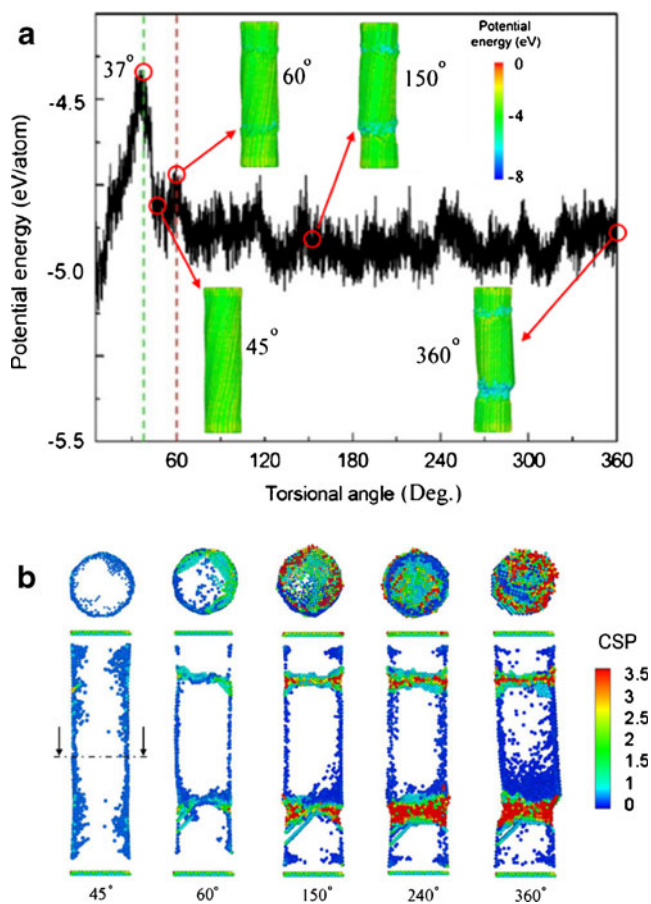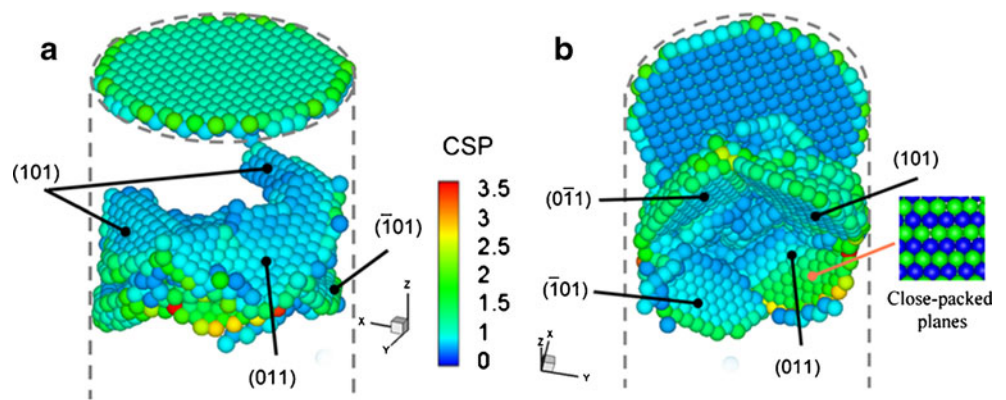

Fig. 2 **a** Variation of average potential energy per atom with θ value. **b** Snapshots of torsional deformation process at a loading rate of 1° ps^{-1} for θ values of 45–360°. The color of atoms represents the magnitude of their CSP

the strain energy through bond breakages of the atoms at the surface. A surface defect appears close to each end when θ reaches 60°, as shown in the snapshots of Fig. 2 (a). With a further increase in the θ value, the energy curve exhibits a repeated cycle with regular oscillation characteristics. This oscillation represents the overcoming of the energy barrier for each dislocation nucleation and stacking. After θ exceeds 150°, the defects extend to the interior and transform into buckling via continuous nucleation and propagation of dislocations. The potential energy of the atoms in the buckling region is relatively low due to the formation of looser amorphous structures. Figure 2 (b) shows the dislocation nucleation and propagation processes within the NW at various θ values. In the initial torsional stage ($\theta < 45°$), dislocations nucleate from the surface. The number of dislocations on the close-packed plane increases with the θ value and the dislocations extend perpendicularly to the NW axis when θ is increased from 45° to 150°. With a further increase in θ (150°– 240°), an increasing number of dislocations meet on a

given plane, leading to the formation of a significant dislocation network. In this period, torsional buckling begins to appear close to the two ends, at which the atoms have high CSP values. Torsional buckling indicates sudden material failure under torsion, which occurs when a material is subjected to a critical amount of torsional deformation. Finally, the dislocation networks become increasingly compact and the NWs accumulate a large number of intrinsic stacking faults. Geometric instability occurs after material instability (buckling), as shown in Fig. 2 (b) (θ=360°). Figures 3 (a) and (b) show snapshots of dislocation nucleation near the top end at θ=55° from different views. The dislocations significantly nucleate on the {110} close-packed plane.

Figure 4 shows the variation of the g(r) function with the θ value. Initially (θ=0°), the g(r) of the NW has high peaks, representing a well-ordered crystal structure. With an increase in the θ value, the g(r) peaks gradually decay. This indicates that the crystal order gradually
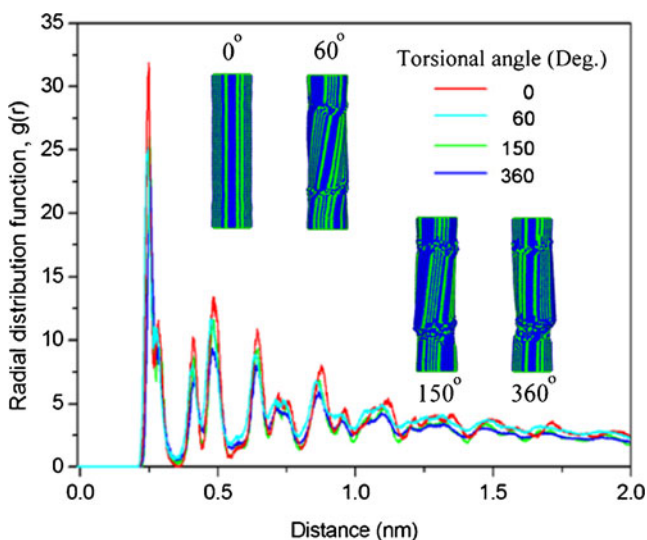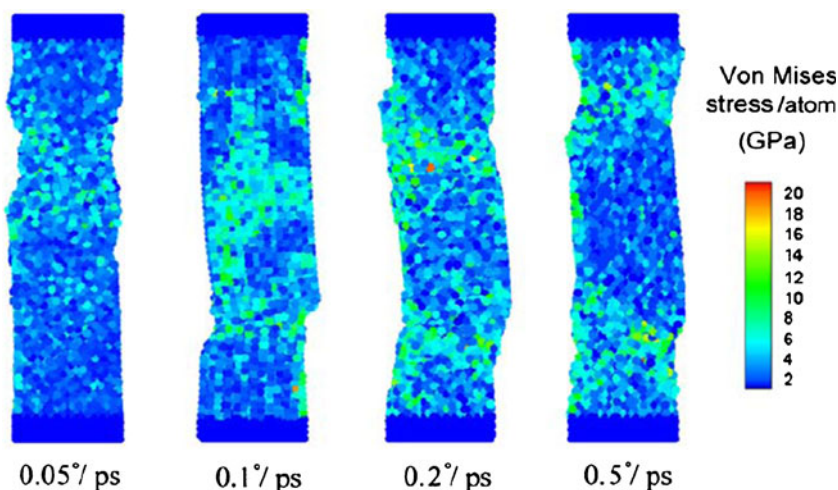

Fig. 4 Variation of radial distribution function with θ value at a loading rate of 1° ps⁻¹

degrades under torsion due to an increase in the number of amorphous structures.

Effect of loading rate

Figure 5 shows the von Mises stress field of the NWs for loading rates of 0.05° ps⁻¹, 0.1° ps⁻¹, 0.2° ps⁻¹, and 0.5° ps⁻¹, respectively, after a total θ of 360°. A NW under torsion with a higher loading rate is subjected to a larger torque for the deformation. With an increase in the loading rate, the occurrence of torsional buckling of a NW is faster, and the buckling gradually develops near the location of the applied external loading. This is due to the atoms in a NW not having sufficient time to release strain energy and rearrange their configuration. Similar results have been found for other metal NWs [26, 27]. The high-stress regions in the NWs correspond to the locations of torsional buckling. The suffered stress increases with the loading rate, as shown in Fig. 5. The middle part of the NW immediately stops rotating during torsional buckling. A regular ordered structure in the middle part of the NW is preserved with a high loading rate. With a decrease in the loading rate, the torsional buckling gradually develops near the middle part of the NW, indicating that the atoms have sufficient time to release accumulated strain energy by adjusting their positions via continuous nucleation and the propagation of dislocations. The mechanism of torsional deformation for a low loading rate is mainly dominated by crystalline dislocation slips and twins, whereas for a high loading rate, it is dominated by the direct transformation from a single-crystal structure to an amorphous structure. The relationship between the deformation mechanism and the loading rate can be determined from the g(r) functions. Figure 6 shows the g(r) function for various loading rates at θ=360°. A short-range order is highly preserved for a low loading rate. With increasing loading rate, the height of the g(r) peaks decreases, indicating the transformation from a single-crystal structure to an amorphous structure. A long-range disorder is

Fig. 5 Snapshots of torsional deformation at $\theta=360°$ at a loading rate of 1° ps^{-1}. Atoms are colored according to the magnitude of their von Mises stress

obvious for a high loading rate due to an increase in the number of amorphous structures.

Effect of aspect ratio

To discuss the effect of the aspect ratio of NWs, L is varied in a range of 10–75 nm, with a constant radius (R) of 2.5 nm, corresponding to aspect ratios (L/R) of 2–15. Figure 7 (a) shows the variations of θ_{cr} and the critical buckling angle (θ_{fl}) with the aspect ratio at a loading rate of 1° ps^{-1}. The θ_{fl} value is the minimum torsional angle at which buckling occurs. The prediction result shows that for a given nanowire with L/R below 5, its θ_{cr} and θ_{fl} values are close. With an increase in the aspect ratio, θ_{cr} and θ_{fl} significantly increase. The θ_{cr} and θ_{fl} values increase in ranges of 15° to 125° and 22° to 150°, respectively, as the aspect ratio is increased from 2 to 15. Similar results have been reported for other metal NWs [25, 27] and carbon

Fig. 6 Variation of radial distribution function with loading rate at $\theta=360°$

nanotubes [28]. This is due to the atoms of a longer NW having more space and freedom to slip and diffuse to release strain energy. The snapshots in Fig. 7 (a) show that a longer NW exhibits larger deflection before buckling. This also indicates that for a long NW, geometric instability occurs before material instability (buckling). Figure 7 (b) shows the variations of the average torque and shear modulus with aspect ratio at a temperature of 300 K and a loading rate of 1° ps^{-1}. The shear modulus (G) is calculated using [29]:

$$\theta = \frac{2TL}{\pi R^4 G}, \qquad (5)$$

where T is the torque before the onset of plastic deformation. For a given NW diameter, the torque required for the deformation gradually decreases and the shear modulus increases with increasing L. This indicates that a longer NW can better resist shear strain by increasing its geometric instability. For bulk materials, however, the shear modulus is a constant, regardless of the length of the crystal. The torque required for the deformation and the shear modulus are in ranges of 480 nN-nm to 509 nN-nm and 72.6 GPa to 127.3 GPa, respectively, as the aspect ratio is increased from 2 to 15. In the simulation, the magnitude of the evaluated shear modulus for NiTi NWs is larger than that for bulk NiTi (52 GPa), which is because the NW with the perfect single-crystal structure has a high theoretical strength. These results indicate a significant size effect on the mechanical properties.
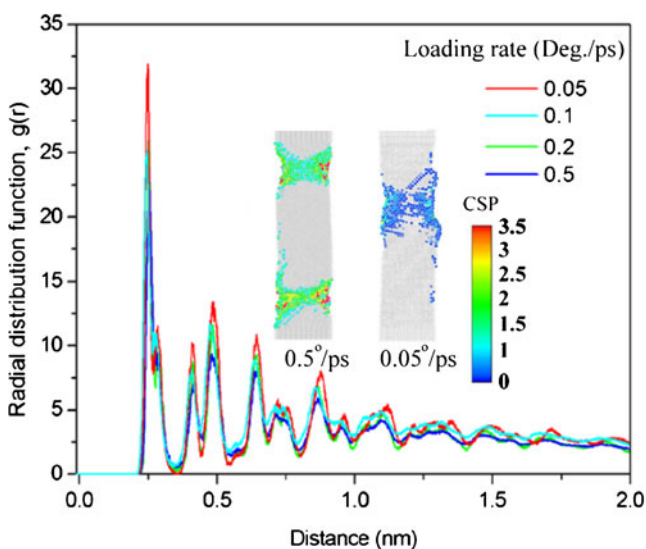
Shape recovery

To clearly observe deformation and shape recovery after unloading, a square NiTi NW with a cross-section area of 19.6 nm^2 is considered, as shown in Fig. 8. The
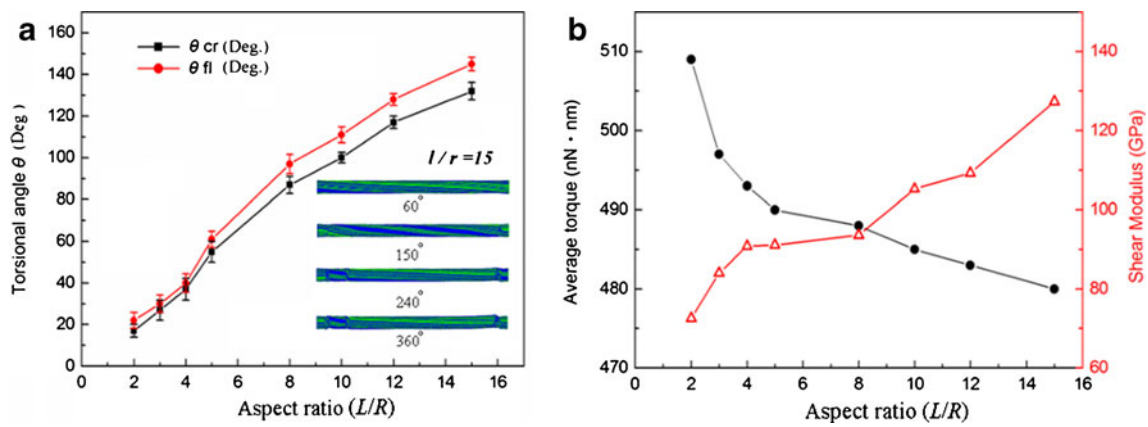
Fig. 7 **a** Variations of critical torsional angle (θ_{cr}) and critical buckling angle (θ_{bkl}) with NW aspect ratio at a loading rate of 1° ps^{-1}. **b** Variations of the average torque and shear modulus with NW aspect ratio

length of the NW is set to 75 nm. For fair comparison, the cross-sectional area of the square NW is the same as that of the circular NWs. Figure 8 (a) shows a series of

torsional deformations of the NW. With an increase in the θ value, the deformation, which twists the surface of the NW around its central axis, increasingly becomes
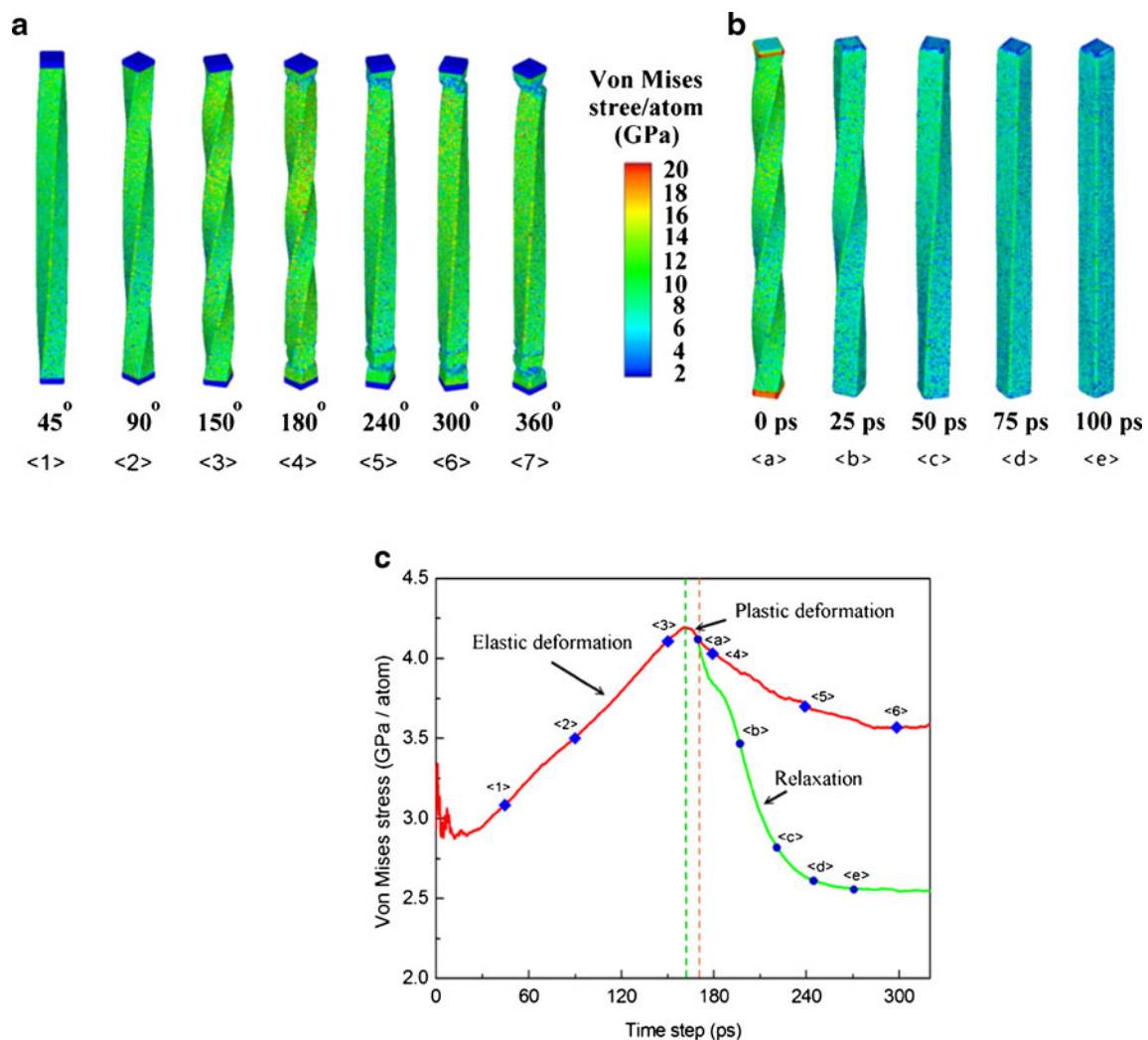

Fig. 8 Snapshots of torsional deformation for **a** θ=45–360° and **b** relaxation at θ=160°. **c** Variation of average potential energy per atom with θ value
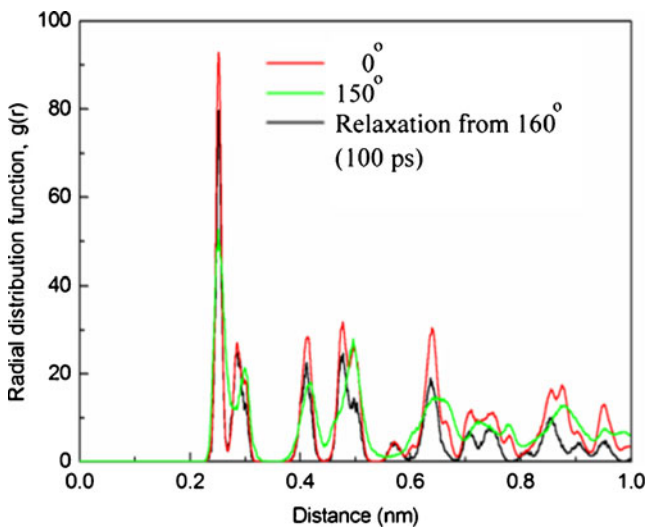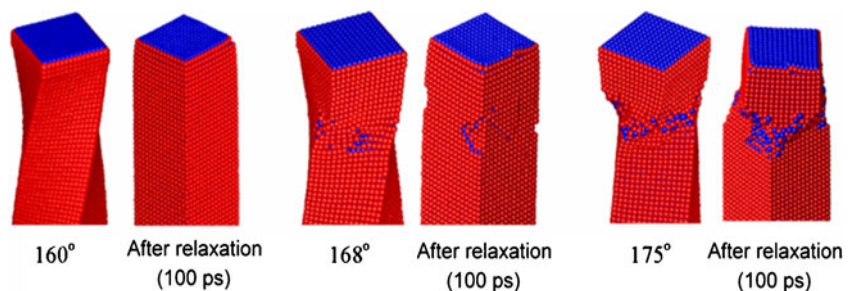
Fig. 9 Profiles of radial distribution function for $\theta=0°$, 150°, and after relaxation from 160°

helical deformation due to stress wave propagation. Compared to the deformation of circular NWs, the deformation of the square NW is more clearly observed due to the effect of shape. However, the deformation mechanism for the two types of NW under torsion is the same. With a further increase in θ, there is a larger amount of helical deformation, at which a further strain energy is stored. The deformed NW suffers a high stress at its center part and remains an ordered crystal structure inside. The maximum amount of helical deformation occurs at $\theta=150\sim180°$. The square NW has an higher mechanical strength than that of the circular NW due to its higher θ_{cr} and θ_{fl} values. Once buckling occurs ($\theta>180°$), the stress propagation from each end to the interior suddenly ends. The large helical deformation and the high stress gradually relax with time via adjustment of interatomic positions. In the following period ($\theta=180\sim240°$), the broken NWs exhibits some shape recovery in order to relax the accumulated strain energy. Figure 8 (b) shows the shape recovery process when the NW is relaxed at $\theta=160°$ (before buckling). The deformed NW completely recovers to its original shape in 100 ps and its internal stress significantly decreases. Figure 8 (c)

shows the variation of the average stress per atom with time for both conditions (Fig. 8 (a) and (b)). At the initial stage, the stress curve exhibits a high and irregular oscillation due to the perfect single-crystal structure under loading. The stress then linearly increases with increasing θ until reaching the critical angle of 160°, which indicates an elastic deformation period. The stress then starts to decay because of plastic deformation. Compared to the case where the deformed NW is relaxed at 160°, the stress decays more quickly, representing a faster shape recovery. The stress relaxation for the broken NW is slower because some strain energies are stored in the defects. As shown in Fig. 8 (a) and (c), the NiTi NW exhibits excellent SE to resist torsional loading. Figure 9 shows the $g(r)$ function for the NW at $\theta=0°$, 150°, and after relaxation from $\theta=160°$. At $\theta=150°$, the short-range order in the deformed NW is partly preserved, which indicates that it has some ordered crystal structure. For the deformed NW relaxed from $\theta=160°$, the height of the $g(r)$ peaks for short-range order increases. A further recovery is expected with longer relaxation. Figure 10 shows the local structure characteristics when the NW is twisted to $\theta=160°$, 168°, and 175° and then relaxed. The results clearly show that great shape recovery is obtained for NiTi NWs before buckling. For example, the shape and the internal crystal structure completely recover after relaxation at 160° (before buckling). However, the shape recovery ability becomes worse with increasing amount of buckling, such as that for cases with relaxation from 168° and 175°.

Conclusions

MD simulations were used to investigate the effects of the loading rate, aspect ratio of NiTi NWs, and NW shape on NW nanomechanical properties, deformation, and shape recovery mechanism. The following conclusions were obtained:

(1) During torsional deformation, dislocation nucleation starts from the surface and extends to the interior along the {110} close-packed plane.

Fig. 10 Developments of local structure for $\theta=160°$, 168°, and 175° followed by relaxation

160°　After relaxation (100 ps)　　168°　After relaxation (100 ps)　　175°　After relaxation (100 ps)

(2) For a high loading rate, the occurrence of torsional buckling of a NW is faster and the buckling gradually develops near the location of the applied external loading.

(3) The critical torsional angle and critical buckling angle increase with the aspect ratio of NWs.

(4) NiTi NWs have great shape recovery before buckling.

References

1. Buehler WJ, Gilfrich JV, Wiley RC (1963) Effect of low–temperature phase changes on the mechanical properties of alloys near composition TiNi. J Appl Phys 34:1475–1477
2. Duerig TW (1990) Engineering aspects of shape memory alloys. Butterworth-Heinemann, London
3. Otsuka K, Wayman CM (1999) Shape memory materials. Cambridge University Press, Cambridge
4. Brailovski V, Prokoshkin S, Terriault P, Trochu F (2003) Shape memory alloys: Fundamentals, modeling and applications. Montreal: ETS Publ
5. Biesiekierski A, Wang J, Gepreel MAH, Wena C (2012) A new look at biomedical Ti-based shape memory alloys. Acta Biomater 8:1661–1669
6. Pequegnat A, Daly M, Wang J, Zhou Y, Khan MI (2012) Dynamic actuation of a novel laser-processed NiTi linear actuator. Smart Mater Struct 21:094004 doi:10.1088/0964-1726/21/9/094004
7. Prokoshkin SD, Khmelevskaya IY, Dobatkin SV, Trubitsyna IB, Tatyanin EV, Stolyarov VV, Prokofiev EA (2005) Alloy composition, deformation temperature, pressure and post-deformation annealing effects in severely deformed Ti-Ni based shape memory alloys. Acta Mater 53:2703–2714
8. Lei X, Rui W, Yong L (2011) The optimization of annealing and cold-drawing in the manufacture of the Ni-Ti shape memory alloy ultra-thin wire. Int J Adv Manuf Technol 55:905–910
9. Chen YF, Sung PH, Wu CD, Fang TH (2012) Studies of nanomechanical properties and fatigue strength of annealed Ni-Ti shape memory alloy. Mater Lett 71:84–87
10. Wu CD, Fang TH, Sung PH, Hsu QC (2012) Recovery, and mechanical property of nanoimprinted Ni-Al alloys investigation using molecular dynamics simulation. Comput Mater Sci 53:321–328
11. Sung PH, Wu CD, Fang TH (2012) Investigation of nanomechanical properties of Al/Ni and Ni/Al nanomultilayers under nanobending using molecular dynamics simulation. Comput Mater Sci 56:43–48
12. Wu CD, Fang TH, Chan CY (2011) A molecular dynamics simulation of the mechanical characteristics of a C60-filled carbon nanotube under nanoindentation using various carbon nanotube tips. Carbon 49:2053–2061
13. Wu CD, Fang TH, Wu TT (2012) Effects of humidity and temperature on laser-assisted dip-pen nanolithography array studied using molecular dynamics simulations. J Colloid Interface Sci 372:170–175
14. Wu CD, Fang TH, Wu TT (2012) Study of process parameters and formative mechanism of patterns on a dip-pen nanolithography array using molecular dynamics simulations. Polymer 53:857–863
15. Zeng ZY, Hu CE, Cai LC, Chen XR, Jing FQ (2011) Molecular dynamics study of the melting curve of NiTi alloy under pressure. J Appl Phys 109:043503
16. Sato T, Saitoh KI, Shinke N (2006) Molecular dynamics study on microscopic mechanism for phase transformation of Ni-Ti alloy. Model Simul Mater Sci Eng 14:39–46
17. Liang W, Srolovitz DJ, Zhou M (2007) A micromechanical continuum model for the tensile behavior of shape memory metal nanowires. J Mech Phys Solids 55:1729–1761
18. Lai WS, Liu BX (2000) Lattice stability of some Ni-Ti alloy phases versus their chemical composition and disordering. J Phys Condens Matter 12:L53–L60
19. Hwang CC, Chang JG, Huang GJ, Huang SH (2001) Investigation of cluster size and cluster incident energy effect on film surface roughness for ionized cluster beam deposition. J Appl Phys 92:5904–5912
20. Haile JM (1992) Molecular dynamics simulation: Elementary methods. Wiley, New York
21. Packeiser D, Gwinner D (1980) The formation mechanisms of dislocation networks in twisted silicon. Philos Mag 42:661–670
22. McClintock FA, Prinz F (1983) A model for the evolution of a twist dislocation network. Acta Metall 31:827–832
23. Gao H, Huang Y, Nix WD, Hutchinson JW (1999) Mechanism-based strain gradient plasticity. I.-Theory. J Mech Phys Solids 47:1239–1263
24. Kelchner CL, Plimpton SJ, Hamilton JC (1998) Dislocation nucleation and defect structure during surface indentation. Phys Rev B 58:11085–11088
25. Jiang S, Zhang H, Zheng Y, Chen Z (2009) Atomistic study of the mechanical response of copper nanowires under torsion. J Phys D Appl Phys 42:135408
26. Gao Y, Wang F, Zhu T, Zhao J (2010) Investigation on the mechanical behaviors of copper nanowires under torsion. Comput Mater Sci 49:826–830
27. Sung PH, Wu CD, Fang TH (2012) Effects of temperature, loading rate, and nanowire length on torsional deformation and mechanical properties of aluminum nanowires investigated using molecular dynamics simulation. J Phys D Appl Phys 45:215303
28. Khoei AR, Ban E, Banihashemi P, Abdolhosseini Qomi MJ (2011) Effects of temperature and torsion speed on torsional properties of single-walled carbon nanotubes. Mater Sci Eng C 31:452–457
29. Leckie FA, Dal Bello DJ (2009) Strength and stiffness of engineering systems. Springer, Heidelberg